Atmospheric
Chemistry
and Physics
Open Access
Discussions

NAT nucleation and denitrification in the Arctic stratosphere

J.-U. Grooß[1], I. Engel[2], S. Borrmann[3,4], W. Frey[4,*], G. Günther[1], C. R. Hoyle[2,5], R. Kivi[6], B. P. Luo[2], S. Molleker[3], T. Peter[2], M. C. Pitts[7], H. Schlager[8], G. Stiller[9], H. Vömel[10], K. A. Walker[11], and R. Müller[1]

[1]Institut für Energie- und Klimaforschung – Stratosphäre (IEK-7), Forschungszentrum Jülich, Germany
[2]Institute for Atmospheric and Climate Science, ETH Zurich, Zurich, Switzerland
[3]Institut für Physik der Atmosphäre, Johannes-Gutenberg-Universität Mainz, Germany
[4]Abteilung Partikelchemie, Max Planck Institut für Chemie, Mainz, Germany
[5]Paul Scherrer Institute, Villigen, Switzerland
[6]Finnish Meteorological Institute, Sodankylä, Finnland
[7]NASA Langley Research Center, Hampton, VA, USA
[8]Institut für Physik der Atmosphäre, Deutsches Zentrum für Luft- und Raumfahrt, Oberpfaffenhofen, Germany
[9]Institute for Meteorology and Climate Research, Karlsruhe Institute of Technology, Karlsruhe, Germany
[10]Meteorological Observatory Lindenberg, Deutscher Wetterdienst, Germany
[11]Department of Physics, University of Toronto, Canada

Discussion Paper | Discussion Paper | Discussion Paper | Discussion Paper

ACPD
13, 22107–22150, 2013

NAT nucleation and denitrification in the Polar stratosphere

J.-U. Grooß et al.

Title Page

Abstract | Introduction
Conclusions | References
Tables | Figures

◄ | ►
◄ | ►

Back | Close

Full Screen / Esc

Printer-friendly Version

Interactive Discussion

*now at: School of Earth Sciences, The University of Melbourne, Melbourne, Australia

NAT nucleation and denitrification in the Polar stratosphere

J.-U. Grooß et al.

Title Page

Abstract	Introduction
Conclusions	References
Tables	Figures

Back   Close

Full Screen / Esc

Printer-friendly Version

Interactive Discussion

Abstract

Nitric acid trihydrate (NAT) particles in the polar stratosphere have been shown to be responsible for vertical redistribution of reactive nitrogen (NO_y). Recent observations by Cloud–Aerosol Lidar with Orthogonal Polarization (CALIOP) aboard the CALIPSO satellite have been explained in terms of heterogeneous nucleation of NAT on foreign nuclei, revealing it to be an important formation pathway for the NAT particles. In state of the art global or regional scale models, heterogeneous NAT nucleation is currently simulated in a very coarse manner using a constant, saturation-independent nucleation rate. Here we present first simulations for the Arctic winter 2009/2010 applying a new saturation-dependent parametrisation of heterogeneous NAT nucleation rates within the Chemical Lagrangian Model of the Stratosphere (CLaMS). The simulation shows good agreement of chemical trace species with in situ and remote sensing observations. The simulated PSC optical properties agree better with CALIOP observations than those simulated with a constant rate model. A comparison of the simulated particle size distributions with observations made using the Forward Scattering Spectrometer Probe (FSSP) aboard the high altitude research aircraft Geophysica, showed that the model reproduces the observed size distribution, except for the very largest particles above 15 µm diameter. The vertical NO_y redistribution caused by the sedimentation of the NAT particles, in particular the denitrification and nitrification signals observed by the ACE-FTS satellite instrument and the in-situ SIOUX instrument aboard the Geophysica, are reproduced by the model, but the improvement of the new parametrisation with respect to the constant rate model remains small.

1 Introduction

It has been known for more than a decade that large nitric acid containing particles of over 10 µm diameter can be present in the cold polar stratosphere (Fahey et al., 2001). These particles are thought to be responsible for the vertical redistribution of NO_y in

the stratosphere, namely denitrification above altitudes of about 18 km and nitrification below. The process of denitrification is important for ozone depletion as it reduces springtime HNO_3 and thus slows down the chlorine deactivation which occurs through the reaction $ClO + NO_2$ at the end of the polar winter (e.g. Müller et al., 1994). Simulations using Lagrangian particle tracking have shown that it is possible to explain the observed denitrification by the vertical HNO_3 transport caused by the sedimentation of these large particles, which are assumed to consist of nitric acid trihydrate (NAT) (Carslaw et al., 2002; Grooß et al., 2005). For these Lagrangian particle trajectories a constant, air-volume based NAT nucleation rate was applied (i.e., constant number of nucleations per time unit per volume of air) whenever temperatures were below T_{NAT}. Besides this on/off dependence for $T < T_{NAT}$ or $T > T_{NAT}$ no other temperature dependence was taken into account because of lacking experimental or observational information (Carslaw et al., 2002; Grooß et al., 2005). For the winter 2002/2003, a simulation with the nucleation rate derived from a single observation, where the NAT nucleation rate in the absence of ice could be constrained (Voigt et al., 2005), reproduced the basic features of the observed denitrification and nitrification (Grooß et al., 2005). However, for other winters a nucleation rate with a three times lower value needed to be chosen to successfully simulate the observed denitrification (Davies et al., 2005).

Recently, studies based on CALIOP data confirmed previous speculations, that heterogeneous nucleation on foreign particles, probably of meteoritic origin, contributes to the NAT nucleation in the polar stratosphere (Hoyle et al., 2013; Engel et al., 2013). Using micro-physical model calculations of the Zurich Optical and Microphysical box Model (ZOMM) along back-trajectories, the saturation-dependence of NAT particle nucleation could be determined (Hoyle et al., 2013). This information is used here to construct a new NAT nucleation parametrisation for the Chemical Lagrangian Model of the Stratosphere (CLaMS).

To this end, we present a comparison between CLaMS simulations and observations for the Arctic winter 2009/2010, in which the extensive measurement campaign of the project RECONCILE (von Hobe et al., 2013) provided detailed measurements. The

Title Page

Abstract | Introduction

Conclusions | References

Tables | Figures

|◄ | ►|

◄ | ►

Back | Close

Full Screen / Esc

Printer-friendly Version

Interactive Discussion

aim of this work is to constrain the value of the NAT nucleation rate by means of PSC observations, especially those by the Cloud–Aerosol Lidar with Orthogonal Polarization (CALIOP) aboard the CALIPSO satellite (Pitts et al., 2009) and in this way improve the simulated denitrification.

Even though the vortex in winter 2009/2010 experienced a vortex split event in early December and was one of the warmest winters within the last two decades, when averaging December–March, the period between mid-December 2009 and end of January 2010 was exceptionally cold (Dörnbrack et al., 2012). During this period, space-borne LIDAR observations by CALIOP indicated more PSCs than in previous Arctic seasons, with significantly more observations of ice clouds and higher number densities of NAT particles than hitherto observed by CALIOP (Pitts et al., 2011).

In addition to the present study, CLaMS has been used in a very similar configuration, however with a constant NAT nucleation rate, in several other recent works examining the Arctic winter of 2009/2010. For example, Hösen (2013) investigated in-situ tracer observations, while Woiwode (2013) and Kalicinsky et al. (2013) used CLaMS to interpret the remote sensing observations of the aircraft instruments MIPAS-ENVISAT and CRISTA-NF, respectively. Further, Wohltmann et al. (2013) performed simulations with a focus on the sensitivity of polar chlorine chemistry and ozone loss on heterogeneous reactions, also using a constant NAT nucleation rate.

2   Model description

2.1   CLaMS

The Chemical Lagrangian Model of the Stratosphere (CLaMS) is a Chemistry Transport Model that is based upon the Lagrangian principle (McKenna et al., 2002a, b; Konopka et al., 2004). The chemical composition of the atmosphere is simulated for multiple air parcels that are moving due to advection. Interaction between the air parcels is realised by an anisotropic mixing scheme (McKenna et al., 2002a; Konopka et al., 2005). The

Back | Close

Full Screen / Esc

Printer-friendly Version

Interactive Discussion

model also includes the Lagrangian simulation of NAT particles (Grooß et al., 2005). Hemispheric simulations starting on 1 December 2009 were carried out using CLaMS with two different spatial resolutions. The reference simulation has a horizontal resolution of 70 km northward of 10° N and 100 km between 0 and 10° N. The vertical model range is between 320 and 900 K, divided into 50 levels, resulting in a vertical resolution of about 450–500 m between 20 and 25 km altitude. This simulation uses about 2.9 million air parcels. Besides this reference simulation, a lower resolution hemispheric configuration was used, with a horizontal resolution of 100 km northward of 40° N, and 300 km southward of 40° N, comparable to earlier simulations, e.g. Grooß and Müller (2007). This configuration uses about 380 000 air parcels in 32 vertical levels and a vertical resolution of about 700 m between 20 and 25 km altitude. It was used for various sensitivity simulations, as described below. Also some evaluations that require large data output were based on the lower resolution configuration.

The underlying wind and temperature fields are taken from the ERA-Interim analysis data provided by the European Centre of Medium-Range Weather Forecasts (ECMWF) (Dee et al., 2011). The CLaMS simulations use a hybrid vertical coordinate ζ, that is equal to potential temperature above the 300 hPa pressure level and transitions to a pressure-like coordinate below (Konopka et al., 2007; Riese et al., 2012). As most of the analysis of this study refers to altitudes above the 300 hPa level, the vertical coordinate ζ can be interpreted here as potential temperature. The vertical velocities are derived from ERA-Interim total diabatic heating rates (Ploeger et al., 2010). For the mixing parametrisation (McKenna et al., 2002a), a time step of 24 h and a critical Lyapunov coefficient of 1.5 day^{-1} were used (Riese et al., 2012).

As micro-physical properties of PSCs are highly temperature-dependent, it is very important to base the simulations on realistic temperature data. Engel et al. (2013) indicated that the ERA-Interim temperature data compared better with the radiosonde observations than other available meteorological analyses. Also, temperature fluctuations occurring on time scales below the 6 h resolution of the ERA-Interim data used here were shown to have a relatively small impact on the NAT nucleation rates (Hoyle

et al., 2013). Further, the effects of such unresolved temperature changes in the model meteorological fields are implicitly accounted for in the NAT nucleation parametrisation.

The CLaMS simulations include dynamical tracers such as passive ozone and passive NO_y, that are not influenced by chemistry. These were initialised at the beginning of the simulations with the ozone and NO_y fields, respectively. The difference between these tracers and their chemically active counterparts can be used to quantify changes due to chemistry or particle sedimentation.

Stratospheric chemistry in CLaMS is an updated version of the scheme described in McKenna et al. (2002b), in which reactions of importance in the upper stratosphere are now included. The 143 reactions of 45 variable chemical species now explicitly contain reactions involving H radicals as well as N_2O and CFCs. The detailed list of reactions included in CLaMS is given in Table A1 in the appendix. Chemical reaction rates and absorption cross sections are based on Sander et al. (2011) including ClOOCl photolysis, which is based on Papanastasiou et al. (2009). Exceptions are the reaction rate for ClOOCl formation which is based on Nickolaisen et al. (1994) and the ClOOCl equilibrium constant which is based on Plenge et al. (2005), respectively, as suggested by Sumińska-Ebersoldt et al. (2012). Heterogeneous reaction rates on liquid aerosol particles are based on the parametrisation of Shi et al. (2001), see also Wegner et al. (2012) for details. As the NAT particles are handled in the separate sedimentation module at locations not congruent with the air parcels, the heterogeneous reactions on the NAT particles could not be considered here, which is justified since it is mostly the liquid particles in the polar stratosphere which are responsible for the heterogeneous reactions leading to the activation of the halogens (Solomon, 1999; Drdla and Müller, 2012; Wegner et al., 2012).

The Lagrangian sedimentation scheme described by Grooß et al. (2005) was used to simulate the vertical redistribution of NO_y. However, the nucleation rate of NAT particles was adapted to the new parametrisation as described below. Within this scheme, the advection of the NAT particles is calculated in a Lagrangian way along individual trajectories. Each particle parcel corresponds to a number of particles with identical

characteristics distributed over a volume equal to the size of the air parcel. To this end, a number concentration is assigned to each particle parcel that is assumed to be constant over that volume. Multiple particle parcels per air parcel are common. The locations for possible NAT nucleation per day were homogeneously distributed in space with a 4 times higher density than that of the air parcels. For a sensitivity study, this ratio between daily nucleating NAT particle parcels and air parcels was increased from 4 to 64 with a decreasing corresponding assigned number density. Growth and evaporation of the individual particles was calculated depending on temperature and gas-phase HNO_3 and H_2O of the neighbouring air parcels. Vertical descent due to sedimentation of the particles is included. The NAT particles are assumed to have the shape of compact spheres.

The dehydration of the stratospheric air masses that typically occurs at the tropopause level is implemented using a temperature-dependent parametrisation for heterogeneous freezing (Krämer et al., 2009; von Hobe et al., 2011). This parametrisation also allows for dehydration in the stratosphere to be simulated similar to that which was observed during January 2010 (Khaykin et al., 2013).

The chemical initialisation of the simulation for 1 December 2009, 12:00 UTC was based on satellite data, on MIPAS-ENVISAT (updated version 5 data from von Clarmann et al. (2009) and ACE-FTS (version 3.0) (Bernath et al., 2005) and observed tracer correlations. Additionally, we used data from a multi-annual CLaMS simulation with simplified chemistry (Pommrich et al., 2011; Ploeger et al., 2013). The details for the individual species are given below.

N_2O was initialised from the multi-annual CLaMS simulation below 400 K and from MIPAS-ENVISAT above 500 K with a linear transition in between. O_3 was initialised above 400 K from MIPAS-ENVISAT data within ±2 days. The observation locations were transformed to the synoptic initialisation time using CLaMS trajectories and gridded to a $2° \times 6°$ grid. Below 350 K, O_3 was taken from the multi-annual simulation with a linear transition in between. Similarly, H_2O was gridded from MIPAS-ENVISAT data above 600 K and taken from the CLaMS multi-annual simulation with a linear transition

NAT nucleation and denitrification in the Polar stratosphere

J.-U. Grooß et al.

in between. The initialisation of CH_4 was derived from N_2O using the correlation from ACE-FTS N_2O and CH_4 data from November 2009 for equivalent latitudes > 65° N. Cl_y and Br_y were derived from CH_4 data correlation after Grooß et al. (2002), where Br_y is increased by 10 % to account for the increase in bromine-containing source gases since the year 2000. Total inorganic nitrogen NO_y could also be initialised from a correlation with N_2O from ACE-FTS data, since ACE-FTS observed all major compounds of NO_y (Jones et al., 2011). For the species CO, CFC-12, CH_3Cl, CFC-22, CCl_4, and CFC-113 a correlation was also derived from ACE-FTS version 3.0 data in November 2009. HNO_3 was derived similarly to O_3 from gridded MIPAS-ENVISAT data, whereas the remaining NO_y species were scaled linearly to fit to the derived total sum of NO_y. CFC-11 mixing ratios were derived from N_2O using data correlation from ACE-FTS version 3.0 for November 2009 and different equivalent latitude ranges (10° S–10° N, 20° N–40° N, 40° N–60° N, and > 60° N). The polynomial fits of all these correlations are listed in Table A2 in the appendix. The remaining minor species as well as the partitioning within the various chemical families are taken from Mainz 2-D model (Grooß, 1996). The sulfate aerosol vertical distribution was initialised consistent with an aerosol surface area density climatology for the months November and December 1998/99, a period with low aerosol particle content (similar to the conditions for the 2009/2010 Arctic winter) from a climatology of D. Considine (Eyring et al., 2006), that is based on SAGE II data for these years.

The boundary conditions at the upper boundary at 900 K were derived from observations similar to the initialisation for two times per month. The mixing ratios of N_2O, H_2O, and HNO_3 were taken from MIPAS-ENVISAT and averaged to equivalent latitude bins. At the lower boundary of the simulations in the free troposphere ($\zeta = 320$ K, corresponding to $\theta = 320$ K within ±5 K at polar latitudes), no modification was made such that the chemical composition an the lower boundary is determined only from the initialisation and transport, predominantly the vertical descent inside the polar vortex.

NAT nucleation and denitrification in the Polar stratosphere

J.-U. Grooß et al.

Title Page

Abstract | Introduction

Conclusions | References

Tables | Figures

|◄ | ►|

◄ | ►

Back | Close

Full Screen / Esc

Printer-friendly Version

Interactive Discussion

2.2 Parametrisation of NAT nucleation

Hoyle et al. (2013) demonstrate that heterogeneous nucleation is needed to explain the occurrence of NAT PSCs observed in the Arctic during the second half of December 2009. A potential source of heterogeneous nuclei is meteoritic dust immersed in stratospheric aerosol particles (Curtius et al., 2005). Hoyle et al. (2013) showed that a constant nucleation rate cannot explain the observed CALIOP PSC data. They assumed that heterogeneous nucleation is triggered by active sites of the individual dust particles and that the nucleation efficiency of these active sites can be characterised by a distribution of contact angles. The occurrence probability distribution of the contact angles is shown in Fig. 2 of Hoyle et al. (2013). For the implementation of the heterogeneous NAT nucleation rates derived in such a way into CLaMS some modifications needed to be made. While in the study of Hoyle et al. (2013), the ZOMM simulations were performed on 10 day back-trajectories that exclusively started at temperatures above T_{NAT}, the nucleation in a chemical transport model must be handled differently. Here we use the 24 h forward air mass trajectories of the CLaMS simulation of which some may start at temperatures below T_{NAT}. The supersaturations required to nucleate a NAT particle in a specific contact angle bin within a 1 h time interval were derived from the parametrisation of Hoyle et al. (2013), which implicitly accounts for the effect of unresolved temperature fluctuations. These values were tabulated to a 2-dimensional array as a function of temperature and 0.1° contact angle bin, as shown in Fig. 1. The right ordinate shows the corresponding dust particle concentrations per contact angle bin taken from Hoyle et al. (2013).

To implement this model into the CLaMS simulation, the history of NAT supersaturation of the air parcels is traced from the time when the temperature falls below T_{NAT}. For that, two additional tracers were introduced to the model that represent the maximum supersaturation of HNO_3 over NAT of an air parcel, S_{NAT}^{max}, and the corresponding temperature T_{min}. The purpose is to trace the information about dust particles in the different contact angle bins that already have been used for NAT particle nucleation. For

each air parcel the maximum NAT supersaturation S_{NAT}^{max} is evaluated for each hour of the following 24 h time interval. For the case that S_{NAT}^{max} is larger than it was at the beginning of the time interval, a positive NAT nucleation rate is determined for this location by summing up the particle concentrations per contact angle bin between the two corre-
5   sponding contact angles before and after the 24 h interval. This number corresponds to the additional dust particles activated for NAT nucleation. Figure 2 is a schematic that illustrates the determination of S_{NAT}^{max}. The hourly calculated values of S_{NAT} are indicated as a red line and the daily determined values of S_{NAT}^{max} as green dots. For this arbitrary example, no additional NAT particles would be nucleated on the last day. Due to the
10   strong non-linearity of the nucleation rate with respect to temperature, we assume that the NAT nucleation rate over one day is dominated by the hour with highest S_{NAT} during the day where the corresponding dust particles are activated and we neglect the nucleation during the rest of the day. As the location of the start of a particle trajectory in general does not coincide with the air parcel, the parametrised nucleation rate is
15   then interpolated onto the locations of NAT particle nucleation in the model. The NAT nucleation rate is then reflected in the NAT number density that is assigned to each individual NAT particle trajectory.

2.3   Sensitivity simulations

To evaluate the dependence of the results on details of this parametrisation and to
20   compare the results with previous simulations, sensitivity simulations were performed, by varying the model parameters.

The labels of these sensitivity simulations given in the discussion below are listed in Table 1. As indicated above, CLaMS simulations were performed either with a high resolution of 70 km north of 10° N (HR) or with a lower resolution of 100 km north of
25   40° N (LR). To test the sensitivity of the results to the number of NAT particle parcels in which NAT could be nucleated, a simulation was performed in which the density of NAT particle parcels nucleated each day was increased from 4 to 64 per air parcel (S64). In turn, the corresponding density assigned to each particle parcel was decreased by

a factor of 16. In a further sensitivity simulation, the NAT nucleation rate was increased by a factor 5 (X5). For comparison with earlier publications we included also a simulation with constant NAT nucleation rate of $8 \times 10^{-6}\,\mathrm{cm}^{-3}\,\mathrm{h}^{-1}$ (Jconst) as used by Grooß et al. (2005), as well as a simulation with the NAT nucleation rate increased by a factor of 10 (Jx10). To investigate the temperature sensitivity, the simulations was also repeated with the ERA-Interim temperatures decreased by 1 K (T-1K).

3 CLaMS results

3.1 Comparison with H_2O and HNO_3 observations

For the simulation of NAT particles it is important to have realistic H_2O and HNO_3 mixing ratios in the simulation. As a rule of thumb for typical polar stratospheric conditions, an increase of 0.5 ppmv H_2O or 3 ppbv HNO_3 introduces a comparable increase to S_{NAT} as a 1 K temperature decrease. Thus, we compared the simulated H_2O and HNO_3 mixing ratios with observations from the balloon based cryogenic frost point hygrometer (CFH), and the satellite based ACE-FTS.

Figure 3 shows four representative comparisons of the model results with balloon based CFH observations made throughout winter, from Sodankylä, Finland (Vömel et al., 2007; Khaykin et al., 2013). Although CLaMS lacks the vertical resolution to reproduce the very fine structure seen in the observations, the large scale features are very well reproduced. The rapid decrease in water vapour above about 300 K is represented well in the model, with only the modelled profile in panel c placing this decrease about 25 K too low. At higher potential temperatures, the model again simulates the increasing water vapour with altitude very well, and even the greater variability of the vertical profile on the 12 March 2010, as shown in panel d appears to be captured to some extent in the CLaMS simulations.

Figure 4 shows the satellite observations of H_2O and HNO_3 obtained by ACE-FTS (average and standard deviation) for the equivalent latitudes above 70° N and time

range 8 January 2010 ± 7 days and the corresponding simulated mixing ratios. This is the first time period during the simulation where latitude coverage of the ACE-FTS satellite observations allows a sufficient number of observations in the vortex core. Again, CLaMS reproduces the observed water vapour values very well, with the only minor deviation from the measurements being the slightly too low altitude reduction in water vapour below 400 K. The upper part of the profile is, however, almost exactly reproduced by the model. The case is similar in the comparison with the ACE-FTS HNO$_3$ measurements. CLaMS captures the general shape and variability of the observed profile extremely well. The small deviations of modelled water vapour from the observations at low altitudes are in an altitude region which will not influence PSC formation. The ability of CLaMS to reproduce the observed H$_2$O and HNO$_3$ fields over the higher regions of the profile suggest that model uncertainty in these fields is unlikely to contribute significantly to any deviations of modelled from observed PSC properties or denitrification.

3.2   Particle size distributions

During the RECONCILE Geophysica campaign, in situ observations of PSCs were obtained during five flights in late January 2010. The size distributions of the PSCs were measured in situ on the Geophysica by the experiments FSSP-100 (1.1–38 µm diameter) and FSSP-300 (0.4–24 µm diameter) (Baumgardner et al., 1992; Borrmann et al., 2000a). Here, we compare the NAT particle simulations with the FSSP observations. Figure 5 shows a comparison with the observations between 11:36 and 11:51 UTC on 22 January 2010. This was the period with the largest particle counts for particles larger than 1 µm diameter. The length of this flight path segment is 167 km at a potential temperature level of 425 K. For the determination of the particle size distribution from CLaMS, the particles within a certain volume need to be combined. This model volume over which the particles are gathered and included in the composition of the size distribution is defined here by up to 100 km distance within this flight path segment and within ±0.5 model level thickness. The sum of particle densities in the individual

particle size bins is divided by the total number of air parcels in the considered volume. The CLaMS results in Fig. 5 show the log-normal distributions assumed for the liquid ternary aerosol as well as the histogram of the NAT particle size distribution. Observations include the FSSP-100 (green symbols) and the FSSP-300 (blue symbols) channel. The log-normal peak of the modelled liquid aerosol corresponds well with the FSSP-300 data that have the better resolution than FSSP-100 towards the lower particle diameter, although the particle phase cannot be derived from FSSP. In the 5–10 µm range, the model somewhat under-estimates the size distribution. Although in the CLaMS simulations, larger NAT particles than during the time of the Geophysica observations do occur in other periods of the winter, reaching median diameters of up to 20 µm, none of these large particles observed on board the Geophysica were present in the model for the time and location of the observational data.

The part of the observed size distribution with very large particles greater than about 15 µm diameter is not present in the simulations as well as not in any of the sensitivity runs. Here the particles are assumed to be compact spheres. One possible cause for this discrepancy could be that the particles are likely to be non-spherical, which could lead to an over-estimation of the observed size (Woiwode, 2013; Borrmann et al., 2000b).

3.3 CALIOP particle classification

A direct comparison of the particles simulated by CLaMS with the CALIOP observations was obtained by simulating the optical signals that would have been caused by the CLaMS particle size distributions. For that purpose, the CLaMS particle size distribution was determined as above for points along the CALIPSO orbit path in the following way: for CALIOP observation profiles with about 25 km spacing along track and 180 m vertical spacing, all CLaMS particle parcels within a reference volume were combined to include enough particles parcels within one air parcel. We assume this volume to be of the order of the average volume of an air parcel in the simulation. This volume is given vertically by one model layer thickness and horizontally by 50 km and 70 km

distance from the point of observation for the high resolution and low resolution runs, respectively. From that volume, a particle size distribution with 15 size bins between 0.8 and 28 µm diameter was determined. In addition, the simulated liquid aerosol particles are characterised by a log-normal distribution. Note that the derived size distributions for neighbouring points are not independent as their reference volumes overlap.

From these particle size distributions, we calculated aerosol backscatter ratios and perpendicular backscatter signals using Mie and T-matrix calculations (Mishchenko et al., 2010). For NAT, we assumed prolate spheroids with aspect ratios of 0.9 (diameter-to-length ratio) and a refractive index of 1.48. Afterwards, the modelled PSCs were classified according to the PSC classification scheme of Pitts et al. (2011). Figures 6 and 7 show the CALIOP results for two selected orbits as well as the corresponding T-matrix calculation results on 21 December and 30 December, respectively. CLaMS results are shown for the simulations Jconst and HR. The observation on 21 December corresponds to a time when the temperatures were low enough to allow the existence of NAT particles for the first few days. It seems that the location of the PSCs and their composition are reproduced in general by the simulation HR, although differences are visible. On 21 December, the extent of the NAT cloud seems to be somewhat under-estimated for the simulation HR, but the simulation Jconst with the constant nucleation rate over-estimates the extent of the PSC. For the CALIOP observation on 30 December the simulation HR also over-estimates the extent of the PSC, however, the simulation Jconst overestimates the observed PSC extent to a far greater degree.

3.4 Vertical redistribution of NO_y

The vertical NO_y redistribution is a direct consequence of the sedimentation of NAT particles. The vertical flux of HNO_3 associated with this sedimentation strongly depends on the size and number of the NAT particles and therefore on the parametrisation of the NAT nucleation rate. Figure 8 shows the vertical HNO_3 flux for the cold time period between late December 2009 and end of January 2010 for the different sensitivity sim-

ulations. This flux is evaluated at the 463 K model level for the area where NAT particles were present in the model. The results for the simulations HR, LR and S64 are almost identical. This shows that the calculated mean HNO_3 flux does not significantly depend on model resolution or the chosen density of model NAT particle parcels. However, significant differences of HNO_3 flux to the other sensitivity simulation occur especially in the early phase (20–25 December) and the late phase (20–30 January). In the simulations with lower temperatures (T-1K) and with constant nucleation rate (Jx10 and Jconst) the onset of HNO_3 flux in late December is earlier and the HNO_3 flux is larger than in the reference simulation for the first 10 days. Differences are also larger towards the end of the cold period. For some sensitivity simulations (Jconst, T-1K) the HNO_3 flux is less than that of the reference run likely because less HNO_3 is available due to earlier denitrification.

The resulting amount of denitrification or nitrification can be deduced by subtracting the passive tracer NO_y^* from the simulated NO_y. The vortex core average of this difference is shown in Fig. 9 as a function of time and the vertical coordinate ζ for the reference run. Clearly visible is the development of a denitrification region above about 425 K and the nitrification peak below where the NAT particles have evaporated. The maximum simulated denitrification reaches 8.5 ppbv on 19 January near 500 K potential temperature. The maximum simulated nitrification was 6 ppbv on 21 January near 400 K potential temperature.

The differences in the vertical NO_y redistribution throughout all simulations is shown in Fig. 10 for two exemplary days. The patterns of denitrification and nitrification are very similar, with the main differences between the model runs being in the magnitude of the denitrification and nitrification, and not in its altitude. In general, larger NAT nucleation rates cause larger amounts of denitrification and nitrification. Due to the lower temperatures in the simulation T-1K, the particles can sediment longer with the consequence that the nitrification peak is about 20 K lower. Around 425 K in mid February, the patterns of denitrification and nitrification at individual locations vary within the sensitivity simulations (not shown). But average profiles, e.g. within the vortex core are very

similar. Especially later in the winter, the difference between the different sensitivity simulations becomes smaller.

A very useful data set to investigate the vertical redistribution of NO_y is the ACE-FTS satellite experiment (Bernath et al., 2005). All major components of NO_y are observed so that the sum NO_y can be determined with high accuracy (Jones et al., 2011). Figure 11 shows the comparison between ACE-FTS version 3.0 and CLaMS for NO_y. Average vortex profiles are shown (equivalent latitudes greater than 70° N) for time periods with a sufficient number of observations within the vortex core. NO_y mixing ratios lower than the passive tracer NO_y^* mixing ratios (grey line) correspond to denitrification and NO_y mixing ratios higher than NO_y^* to nitrification. Model results for the new nucleation parametrisation as well as for constant nucleation rates are shown, for four time periods in which ACE-FTS observation latitudes cover the Arctic region. In early January, the process of vertical NO_y redistribution starts with less than about 1–2 ppbv denitrification and nitrification. The HR simulation closely reproduces the observed NO_y, with a slight underestimation at around 475 K. The simulation Jconst produced similar results, however with a slight overestimation at around 575 K and a greater underestimation at 475 K than the simulation HR. Jx10 produces a too severe denitrification. During the end of January and early February, a severe denitrification of over 5 ppbv and a distinct nitrification layer is present in both observational and simulated data. For the end of January, the observed profile is best represented by the Jx10 simulation, while both HR and Jconst show too much NO_y throughout most of the profile. For mid February however, HR again provides the best representation of the observations, with Jconst giving very similar results, and Jx10 again underestimating the NO_y throughout most of the column. In early March, the signature of the nitrification layer decreased due to mixing with air unaffected by nitrification, whereby the denitrification signature is smoothed out but is still visible. Both the HR and Jconst runs reproduce the observed profile well, with Jx10 underestimating NO_y throughout the profile.

The simulated NO_y redistribution was also compared with gas-phase in situ NO_y observations made from the Stratospheric Observation Unit for Nitrogen Oxide (SIOUX)

NAT nucleation and denitrification in the Polar stratosphere

J.-U. Grooß et al.

Title Page

Abstract	Introduction
Conclusions	References
Tables	Figures

|◀ | ▶|

| ◀ | ▶ |

| Back | Close |

Full Screen / Esc

Printer-friendly Version

Interactive Discussion

aboard the Geophysica aircraft (Voigt et al., 2005). Generally, the SIOUX observations during the RECONCILE campaign show both denitrification and the nitrification layer. An evaluation of the simulated NO_y is however difficult since there are small-scale structures below the model resolution that cannot be reproduced. Figure 12 shows the comparison for four flight segments in which SIOUX NO_y observations within the vortex have been made. The observations are compared with the sensitivity simulations with high and low resolution (HR, LR) and the simulation with 1 K temperatures decrease (T-1K). The flights on 30 January and 2 February are located at the transition between the denitrification and the nitrification region (compare Fig. 9). The flight on 30 January was the so-called self-match flight (Sumińska-Ebersoldt et al., 2012) that attempted to probe the same air masses twice resulting in mirroring data structures before and after about 8:20 UTC (dotted line Fig. 12a). The symmetry before and after the turnaround point is visible in the data and also in the model results. But the agreement between model versions and data here are not very good. For 30 January and 2 February, a very detailed small scale structure of NO_y is visible both in the observations and in the model. However, the small-scale structure is not reproduced in detail and also the individual sensitivity runs show different structures among themselves. Especially significant differences can be seen between the runs with different spatial resolutions (HR, LR) that is not seen in the other comparisons. Even in the HR run, the smallest structures in this region cannot be resolved in every detail, probably because small differences in winds or temperatures below the accuracy of the ERA-INTERIM data cause relevant differences in the location of particle evaporation. It should be noted however, that the global results as zonal mean or vortex mean profiles of NO_y or HNO_3 flux agree quite well for the two resolutions. On 2 March, a vortex remnant was observed in the vicinity of Spitsbergen between about 10:00 and 11:00 UTC, where all the performed simulations under-estimate the observed denitrification. On 10 March, when observations within the vortex were taken at somewhat higher potential temperature, the results of the different simulations are closer together and comparable with the observations. Between about 08:50 and 09:20 UTC the observations are located outside the vortex.

A filament of extra-vortex air that was recently drawn into the vortex observed around 8:30 UTC (Hösen, 2013) marked by the dotted lines shows no denitrification which can be deduced from NO_y^*.

The altitude dependence of the NO_y redistribution is shown similarly in Fig. 13 for
5 flights on 4 different days with altitude profiles containing the nitrification peak. The simulations reproduce the general features like the denitrification region and the nitrification peak. However, also the small-scale variability can not be reproduced in every detail as explained above. The evaluation of the simulated vertical NO_y redistribution and the comparison with ACE-FTS and SIOUX data indicates that the sensitivity on
10 the choice of nucleation rate parametrisation in early March is less pronounced than in January.

4 Conclusions

We have shown global model simulations of NAT particle nucleation, particle growth, sedimentation and resulting denitrification. For the first time, a temperature-dependent
15 NAT nucleation rate, derived from CALIOP observations (Hoyle et al., 2013; Engel et al., 2013) has been applied to a global chemical transport model. The processes leading to denitrification have been compared with observations including CALIOP particle classification, observed size distributions and observations of NO_y and its compounds by various observational techniques and platforms. The comparisons show that
20 the general behaviour of the observations is reproduced by the simulations. The locations and extent of the observed NAT PSCs as seen in the CALIOP data are generally better reproduced by the new nucleation scheme than by using a constant nucleation rate. The model configuration employing the new NAT nucleation parametrisation reproduces the vortex averaged NO_y profiles observed by ACE-FTS slightly better than
25 the version based on the constant rate based NAT nucleation parametrisation. However, deviations between observations and the simulation are still evident. These differences can be due to various reasons, including small-scale temperature fluctuations

and temperature biases, non-sphericity of the NAT particles, model initialisation, and the nucleation rate related assumptions. Sensitivity studies with respect to model resolution and analysed temperature show areas where the actual structure of NO_y redistribution cannot be exactly simulated, where the results in mid-March are less sensitive to the model uncertainties than the results for the beginning of the PSC period. Especially during the setup of the PSC period, the differences of the new method proposed here with respect to using a constant NAT nucleation rate are large.

The numerical cost of the new parametrisation is similar to using a constant nucleation rate. As there is a slight improvement in the modelled denitrification with the new parametrisation, and also because a NAT saturation dependent parametrisation is more realistic than assuming a constant rate, we propose that the new parametrisation is used in future studies of PSC formation and denitrification. In future studies on the basis of more observational data, it may be possible to better attribute the remaining differences between observations and model results to specific processes in the model, such as sedimentation rates, or to specific uncertainties in the measurements.

Appendix A

CLaMS model details

The chemical reaction scheme has been updated with respect to McKenna et al. (2002b) and the additional reactions are listed in Table A1. The polynomial fits of the correlations used in the initialisation and boundary condition are summarised in Table A2.

References

Baumgardner, D., Dye, J. E., Gandrud, B. W., and Knollenberg, R. G.: Interpretation of measurements made the Forward Scattering Spectrometer Probe (FSSP300) during the airborne artic stratospheric expedition, J. Geophys. Res., 97, 8035–8046, 1992. 22119

Bernath, P. F., McElroy, C. T., Abrams, M. C., Boone, C. D., Butler, M., Camy-Peyret, C., Carleer, M., Clerbaux, C., Coheur, P.-F., Colin, R., DeCola, P., DeMazière, M., Drummond, J. R., Dufour, D., Evans, W. F. J., Fast, H., Fussen, D., Gilbert, K., Jennings, D. E., Llewellyn, E. J., Lowe, R. P., Mahieu, E., McConnell, J. C., McHugh, M., McLeod, S. D., Michaud, R., Midwinter, C., Nassar, R., Nichitiu, F., Nowlan, C., Rinsland, C. P., Rochon, Y. J., Rowlands, N., Semeniuk, K., Simon, P., Skelton, R., Sloan, J. J., Soucy, M.-A., Strong, K., Tremblay, P., Turnbull, D., Walker, K. A., Walkty, I., Wardle, D. A., Wehrle, V., Zander, R., and Zou, J.: Atmospheric Chemistry Experiment (ACE) mission overview, Geophys. Res. Lett., 32, L15S01, doi:10.1029/2005GL022386, 2005. 22114, 22123

Borrmann, S., Thomas, A., Rudakov, V., Yushkov, V., Lepuchov, B., Deshler, T., Vinnichenko, N., Khattatov, V., and Stefanutti, L.: Stratospheric aerosol measurements in the Arctic winter of 1996/1997 with the M-55 Geophysika high-altitude research aircraft, Tellus B, 52, 1088–1103, doi:10.1034/j.1600-0889.2000.00100.x, 2000a. 22119

Borrmann, S., Luo, B., and Mishchenko, M.: Application of the T-matrix method to the measurement of aspherical (ellipsoidal) particles with forward scattering optical particle counters, J. Aerosol Sci., 31, 789–799, doi:10.1016/S0021-8502(99)00563-7, 2000b. 22120

Carslaw, K. S., Kettleborough, J. A., Northway, M. J., Davies, S., Gao, R., Fahey, D. W., Baumgardner, D. G., Chipperfield, M. P., and Kleinböhl, A.: A vortex-scale simulation of the growth and sedimentation of large nitric acid hydrate particles, J. Geophys. Res., 107, 8300, doi:10.1029/2001JD000467, 2002. 22110

5 Curtius, J., Weigel, R., Vössing, H.-J., Wernli, H., Werner, A., Volk, C.-M., Konopka, P., Krebs-bach, M., Schiller, C., Roiger, A., Schlager, H., Dreiling, V., and Borrmann, S.: Observations of meteoric material and implications for aerosol nucleation in the winter Arctic lower strato-sphere derived from in situ particle measurements, Atmos. Chem. Phys., 5, 3053–3069, doi:10.5194/acp-5-3053-2005, 2005. 22116

10 Davies, S., Mann, G. W., Carslaw, K. S., Chipperfield, M. P., Kettleborough, J. A., Santee, M. L., Oelhaf, H., Wetzel, G., Sasano, Y., and Sugita, T.: 3-D microphysical model studies of Arctic denitrification: comparison with observations, Atmos. Chem. Phys., 5, 3093–3109, doi:10.5194/acp-5-3093-2005, 2005. 22110

Dee, D. P., Uppala, S. M., Simmons, A. J., Berrisford, P., Poli, P., Kobayashi, S., Andrae, U.,
15 Balmaseda, M. A., Balsamo, G., Bauer, P., Bechtold, P., Beljaars, A. C. M., van de Berg, L., Bidlot, J., Bormann, N., Delsol, C., Dragani, R., Fuentes, M., Geer, A. J., Haimberger, L., Healy, S. B., Hersbach, H., Holm, E. V., Isaksen, L., Kallberg, P., Koehler, M., Matricardi, M., McNally, A. P., Monge-Sanz, B. M., Morcrette, J. J., Park, B. K., Peubey, C., de Ros-nay, P., Tavolato, C., Thepaut, J. N., and Vitart, F.: The ERA-Interim reanalysis: configuration
20 and performance of the data assimilation system, Q. J. Roy. Meteor. Soc., 137, 553–597, doi:10.1002/qj.828, 2011. 22112

Dörnbrack, A., Pitts, M. C., Poole, L. R., Orsolini, Y. J., Nishii, K., and Nakamura, H.: The 2009–2010 Arctic stratospheric winter – general evolution, mountain waves and predictability of an operational weather forecast model, Atmos. Chem. Phys., 12, 3659–3675, doi:10.5194/acp-
25 12-3659-2012, 2012. 22111

Drdla, K. and Müller, R.: Temperature thresholds for chlorine activation and ozone loss in the polar stratosphere, Ann. Geophys., 30, 1055–1073, doi:10.5194/angeo-30-1055-2012, 2012. 22113

Engel, I., Luo, B. P., Pitts, M. C., Poole, L. R., Hoyle, C. R., Grooß, J.-U., Dörnbrack, A., and
30 Peter, T.: Heterogeneous formation of polar stratospheric clouds – Part 2: Nucleation of ice on synoptic scales, Atmos. Chem. Phys. Discuss., 13, 8831–8872, doi:10.5194/acpd-13-8831-2013, 2013. 22110, 22112, 22125

Title Page

Abstract | Introduction

Conclusions | References

Tables | Figures

|◄ | ►|

◄ | ►

Back | Close

Full Screen / Esc

Printer-friendly Version

Interactive Discussion

Eyring, V., Butchart, N., Waugh, D. W., Akiyoshi, H., Austin, J., Bekki, S., Bodeker, G. E., Boville, B. A., Brühl, C., Chipperfield, M. P., Cordero, E., Dameris, M., Deushi, M., Fioletov, V. E., Frith, S. M., Garcia, R. R., Gettelman, A., Giorgetta, M. A., Grewe, V., Jourdain, L., Kinnison, D. E., Mancini, E., Manzini, E., Marchand, M., Marsh, D. R., Nagashima, T., Nielsen, E., Newman, P. A., Pawson, S., Pitari, G., Plummer, D. A., Rozanov, E., Schraner, M., Shepherd, T. G., Shibata, K., Stolarski, R. S., Struthers, H., Tian, W., and Yoshiki, M.: Assessment of temperature, trace species and ozone in chemistry-climate simulations of the recent past, J. Geophys. Res., 111, D22308, doi:10.1029/2006JD007327, 2006. 22115

Fahey, D. W., Gao, R. S., Carslaw, K. S., Kettleborough, J., Popp, P. J., Northway, M. J., Holecek, J. C., Ciciora, S. C., McLaughlin, R. J., Thompson, T. L., Winkler, R. H., Baumgardner, D. G., Gandrud, B., Wennberg, P. O., Dhaniyala, S., McKinley, K., Peter, T., Salawitch, R. J., Bui, T. P., Elkins, J. W., Webster, C. R., Atlas, E. L., Jost, H., Wilson, J. C., Herman, R. L., Kleinböhl, A., and von König, M.: The detection of large HNO_3-containing particles in the winter Arctic stratosphere, Science, 291, 1026–1031, 2001. 22109

Grooß, J.-U.: Modelling of Stratospheric Chemistry based on HALOE/UARS Satellite Data, PhD thesis, University of Mainz, 1996. 22115

Grooß, J.-U. and Müller, R.: Simulation of ozone loss in Arctic winter 2004/2005, Geophys. Res. Lett., 34, L05804, doi:10.1029/2006GL028901, 2007. 22112

Grooß, J.-U., Günther, G., Konopka, P., Müller, R., McKenna, D. S., Stroh, F., Vogel, B., Engel, A., Müller, M., Hoppel, K., Bevilacqua, R., Richard, E., Webster, C. R., Elkins, J. W., Hurst, D. F., Romashkin, P. A., and Baumgardner, D. G.: Simulation of ozone depletion in spring 2000 with the Chemical Lagrangian Model of the Stratosphere (CLaMS), J. Geophys. Res., 107, 8295, doi:10.1029/2001JD000456, 2002. 22115

Grooß, J.-U., Günther, G., Müller, R., Konopka, P., Bausch, S., Schlager, H., Voigt, C., Volk, C.M., and Toon, G. C.: Simulation of denitrification and ozone loss for the Arctic winter 2002/2003, Atmos. Chem. Phys., 5, 1437–1448, doi:10.5194/acp-5-1437-2005, 2005. 22110, 22112, 22113, 22118, 22137

Hösen, E.: Untersuchung von Transport, Mischung und Ozonverlust in der arktischen Polarregion im Winter 2009/10 basierend auf flugzeuggestützten in-situ-Messungen, Dissertation, Bergische Universität Wuppertal, Germany, 2013. 22111, 22125

Hoyle, C. R., Engel, I., Luo, B. P., Pitts, M. C., Poole, L. R., Grooß, J.-U., and Peter, T.: Heterogeneous formation of polar stratospheric clouds – Part 1: Nucleation of nitric acid tri-

NAT nucleation and denitrification in the Polar stratosphere

J.-U. Grooß et al.

hydrate (NAT), Atmos. Chem. Phys. Discuss., 13, 7979–8021, doi:10.5194/acpd-13-7979-2013, 2013. 22110, 22112, 22116, 22125, 22138

Jones, A., Qin, G., Strong, K., Walker, K. A., McLinden, C., M. Toohey, T., Kerzenmacher, Bernath, P., and Boone, C.: A global inventory of stratospheric NO_y from ACE-FTS, J. Geophys. Res., 116, D17304, doi:10.1029/2010JD015465, 2011. 22115, 22123

Kalicinsky, C., Grooß, J.-U., Günther, G., Ungermann, J., Blank, J., Höfer, S., Hoffmann, L., Knieling, P., Olschewski, F., Spang, R., Stroh, F., and Riese, M.: Small-scale transport structures in the Arctic winter 2009/2010, Atmos. Chem. Phys. Discuss., 13, 10463–10498, doi:10.5194/acpd-13-10463-2013, 2013. 22111

Khaykin, S. M., Engel, I., Vömel, H., Formanyuk, I. M., Kivi, R., Korshunov, L. I., Krämer, M., Lykov, A. D., Meier, S., Naebert, T., Pitts, M. C., Santee, M. L., Spelten, N., Wienhold, F. G., Yushkov, V. A., and Peter, T.: Arctic stratospheric dehydration – Part 1: Unprecedented observation of vertical redistribution of water, Atmos. Chem. Phys. Discuss., 13, 14249–14295, doi:10.5194/acpd-13-14249-2013, 2013. 22114, 22118

Konopka, P., Steinhorst, H.-M., Grooß, J.-U., Günther, G., Müller, R., Elkins, J. W., Jost, H.-J., Richard, E., Schmidt, U., Toon, G., and McKenna, D. S.: Mixing and ozone loss in the 1999–2000 Arctic Vortex: simulations with the 3-dimensional Chemical Lagrangian Model of the Stratosphere (CLaMS), J. Geophys. Res., 109, D02315, doi:10.1029/2003JD003792, 2004. 22111

Konopka, P., Günther, G., McKenna, D. S., Müller, R., Offermann, D., Spang, R., and Riese, M.: How homogeneous and isotropic is stratospheric mixing? Comparison of CRISTA-1 observations with transport studies based on the Chemical Lagrangian Model of the Stratosphere (CLaMS), Q. J. Roy. Meteor. Soc., 131, 565–579, doi:10.1256/qj.04.47, 2005. 22111

Konopka, P., Günther, G., Müller, R., dos Santos, F. H. S., Schiller, C., Ravegnani, F., Ulanovsky, A., Schlager, H., Volk, C. M., Viciani, S., Pan, L. L., McKenna, D.-S., and Riese, M.: Contribution of mixing to upward transport across the tropical tropopause layer (TTL), Atmos. Chem. Phys., 7, 3285–3308, doi:10.5194/acp-7-3285-2007, 2007. 22112

Krämer, M., Schiller, C., Afchine, A., Bauer, R., Gensch, I., Mangold, A., Schlicht, S., Spelten, N., Sitnikov, N., Borrmann, S., de Reus, M., and Spichtinger, P.: Ice supersaturations and cirrus cloud crystal numbers, Atmos. Chem. Phys., 9, 3505–3522, doi:10.5194/acp-9-3505-2009, 2009. 22114

McKenna, D. S., Konopka, P., Grooß, J.-U., Günther, G., Müller, R., Spang, R., Offermann, D., and Orsolini, Y.: A new Chemical Lagrangian Model of the Stratosphere (CLaMS): 1. For-

Title Page

Abstract | Introduction

Conclusions | References

Tables | Figures

|◄ | ►|

◄ | ►

Back | Close

Full Screen / Esc

Printer-friendly Version

Interactive Discussion

mulation of advection and mixing, J. Geophys. Res., 107, 4309, doi:10.1029/2000JD000114, 2002a. 22111, 22112

McKenna, D. S., Grooß, J.-U., Günther, G., Konopka, P., Müller, R., Carver, G., and Sasano, Y.: A new Chemical Lagrangian Model of the Stratosphere (CLaMS): 2. Formulation of chemistry scheme and initialization, J. Geophys. Res., 107, 4256, doi:10.1029/2000JD000113, 2002b. 22111, 22113, 22126, 22136

Mishchenko, M. I., Travis, L. D., and Mackowski, D. W.: T-matrix computations of light scattering by nonspherical particles: a review, J. Quant. Spectrosc. Radiat. Transf., 111, 1704–1744, 2010. 22121

Müller, R., Peter, T., Crutzen, P. J., Oelhaf, H., Adrian, G. P., v. Clarmann, T., Wegner, A., Schmidt, U., and Lary, D.: Chlorine chemistry and the potential for ozone depletion in the Arctic stratosphere in the winter of 1991/92, Geophys. Res. Lett., 21, 1427–1430, 1994. 22110

Nickolaisen, S. L., Friedl, R. R., and Sander, S. P.: Kinetics and mechanism of the ClO + ClO reaction – pressure and temperature dependences of the bimolecular and termolecular channels and thermal-decomposition of chlorine peroxide, J. Phys. Chem., 98, 155–169, 1994. 22113

Papanastasiou, D. K., Papadimitriou, V. C., Fahey, D. W., and Burkholder, J. B.: UV absorption spectrum of the ClO dimer (Cl_2O_2) between 200 and 420 nm, J. Phys. Chem. A, 113, 13711–13726, 2009. 22113

Pitts, M. C., Poole, L. R., and Thomason, L. W.: CALIPSO polar stratospheric cloud observations: second-generation detection algorithm and composition discrimination, Atmos. Chem. Phys., 9, 7577–7589, doi:10.5194/acp-9-7577-2009, 2009. 22111, 22143

Pitts, M. C., Poole, L. R., Dörnbrack, A., and Thomason, L. W.: The 2009–2010 Arctic polar stratospheric cloud season: a CALIPSO perspective, Atmos. Chem. Phys., 11, 2161–2177, doi:10.5194/acp-11-2161-2011, 2011. 22111, 22121

Plenge, J., Kühl, S., Vogel, B., Müller, R., Stroh, F., von Hobe, M., Flesch, R., and Rühl, E.: Bond strength of chlorine peroxide, J. Phys. Chem. A, 109, 6730–6734, 2005. 22113

Ploeger, F., Konopka, P., Günther, G., Grooß, J.-U., and Müller, R.: Impact of the vertical velocity scheme on modeling transport across the tropical tropopause layer, J. Geophys. Res., 115, D03301, doi:10.1029/2009JD012023, 2010. 22112

Ploeger, F., Günther, G., Konopka, P., Fueglistaler, S., Müller, R., Hoppe, C., Kunz, A., Spang, R., Grooß, J.-U., and Riese, M.: Horizontal water vapor transport in the lower strato-

sphere from subtropics to high latitudes during boreal summer, J. Geophys. Res., 118, 8111–8127, doi:10.1002/jgrd.50636, 2013. 22114

Pommrich, R., Müller, R., Grooß, J.-U., Konopka, P., Günther, G., Pumphrey, H.-C., Viciani, S., D'Amato, F., and Riese, M.: Carbon monoxide as a tracer for tropical troposphere to stratosphere transport in the Chemical Lagrangian Model of the Stratosphere (CLaMS), Geosci. Model Dev. Discuss., 4, 1185–1211, doi:10.5194/gmdd-4-1185-2011, 2011. 22114

Riese, M., Ploeger, F., Rap, A., Vogel, B., Konopka, P., Dameris, M., and Forster, P.: Impact of uncertainties in atmospheric mixing on simulated UTLS composition and related radiative effects, J. Geophys. Res., 117, D16305 doi:10.1029/2012JD017751, 2012. 22112

Sander, S. P., Friedl, R. R., Barker, J. R., Golden, D. M., Kurylo, M. J., Wine, P. H., Abbatt, J. P. D., Burkholder, J. B., Kolb, C. E., Moortgat, G. K., Huie, R. E., and Orkin, V. L.: Chemical Kinetics and Photochemical Data for Use in Atmospheric Studies, JPL Publication 10-6, 2011. 22113

Shi, Q., Jayne, J. T., Kolb, C. E., Worsnop, D. R., and Davidovits, P.: Kinetic model for reaction of $ClONO_2$ with H_2O and HCl and HOCl with HCl in sulfuric acid solutions, J. Geophys. Res., 106, 24259–24274, doi:10.1029/2000JD000181, 2001. 22113

Solomon, S.: Stratospheric ozone depletion: a review of concepts and history, Rev. Geophys., 37, 275–316, doi:10.1029/1999RG900008, 1999. 22113

Sumińska-Ebersoldt, O., Lehmann, R., Wegner, T., Grooß, J.-U., Hösen, E., Weigel, R., Frey, W., Griessbach, S., Mitev, V., Emde, C., Volk, C. M., Borrmann, S., Rex, M., Stroh, F., and von Hobe, M.: ClOOCl photolysis at high solar zenith angles: analysis of the RECONCILE self-match flight, Atmos. Chem. Phys., 12, 1353–1365, doi:10.5194/acp-12-1353-2012, 2012. 22113, 22124

Voigt, C., Schlager, H., Luo, B. P., Dörnbrack, A., Roiger, A., Stock, P., Curtius, J., Vössing, H., Borrmann, S., Davies, S., Konopka, P., Schiller, C., Shur, G., and Peter, T.: Nitric Acid Trihydrate (NAT) formation at low NAT supersaturation in Polar Stratospheric Clouds (PSCs), Atmos. Chem. Phys., 5, 1371–1380, doi:10.5194/acp-5-1371-2005, 2005. 22110, 22124

Vömel, H., David, D. E., and Smith, K.: Accuracy of tropospheric and stratospheric water vapor measurements by the cryogenic frost point hygrometer: instrumental details and observations, J. Geophys. Res., 112, D08305 doi:10.1029/2006JD007224, 2007. 22118

von Clarmann, T., Höpfner, M., Kellmann, S., Linden, A., Chauhan, S., Funke, B., Grabowski, U., Glatthor, N., Kiefer, M., Schieferdecker, T., Stiller, G. P., and Versick, S.: Retrieval of temperature, H_2O, O_3, HNO_3, CH_4, N_2O, $ClONO_2$ and ClO from MIPAS reduced resolution nominal

NAT nucleation and denitrification in the Polar stratosphere

J.-U. Grooß et al.

Title Page

Abstract	Introduction
Conclusions	References
Tables	Figures

◀ | ▶

◀ | ▶

Back | Close

Full Screen / Esc

Printer-friendly Version

Interactive Discussion

mode limb emission measurements, Atmos. Meas. Tech., 2, 159–175, doi:10.5194/amt-2-159-2009, 2009. 22114

von Hobe, M., Grooß, J.-U., Günther, G., Konopka, P., Gensch, I., Krämer, M., Spelten, N., Afchine, A., Schiller, C., Ulanovsky, A., Sitnikov, N., Shur, G., Yushkov, V., Ravegnani, F., Cairo, F., Roiger, A., Voigt, C., Schlager, H., Weigel, R., Frey, W., Borrmann, S., Müller, R., and Stroh, F.: Evidence for heterogeneous chlorine activation in the tropical UTLS, Atmos. Chem. Phys., 11, 241–256, doi:10.5194/acp-11-241-2011, 2011. 22114

von Hobe, M., Bekki, S., Borrmann, S., Cairo, F., D'Amato, F., Dörnbrack, A., Ebersoldt, A., Ebert, M., Emde, C., Engel, I., Ern, M., Frey, W., Genco, S., Griessbach, S., Grooß, J.-U., Gulde, T., Günther, G., Hösen, E., Hoffmann, L., Homonnai, V., Hoyle, C. R., Isaksen, I. S. A., Jackson, D. R., Jánosi, I. M., Jones, R. L., Kandler, K., Kalicinsky, C., Keil, A., Khaykin, S. M., Khosrawi, F., Kivi, R., Kuttippurath, J., Laube, J. C., Lefèvre, F., Lehmann, R., Ludmann, S., Luo, B. P., Marchand, M., Meyer, J., Mitev, V., Molleker, S., Müller, R., Oelhaf, H., Olschewski, F., Orsolini, Y., Peter, T., Pfeilsticker, K., Piesch, C., Pitts, M. C., Poole, L. R., Pope, F. D., Ravegnani, F., Rex, M., Riese, M., Röckmann, T., Rognerud, B., Roiger, A., Rolf, C., Santee, M. L., Scheibe, M., Schiller, C., Schlager, H., Siciliani de Cumis, M., Sitnikov, N., Søvde, O. A., Spang, R., Spelten, N., Stordal, F., Sumińska-Ebersoldt, O., Ulanovsky, A., Ungermann, J., Viciani, S., Volk, C. M., vom Scheidt, M., von der Gathen, P., Walker, K., Wegner, T., Weigel, R., Weinbuch, S., Wetzel, G., Wienhold, F. G., Wohltmann, I., Woiwode, W., Young, I. A. K., Yushkov, V., Zobrist, B., and Stroh, F.: Reconciliation of essential process parameters for an enhanced predictability of Arctic stratospheric ozone loss and its climate interactions (RECONCILE): activities and results, Atmos. Chem. Phys., 13, in press, 2013. 22110

Wegner, T., Grooß, J.-U., von Hobe, M., Stroh, F., Sumińska-Ebersoldt, O., Volk, C. M., Hösen, E., Mitev, V., Shur, G., and Müller, R.: Heterogeneous chlorine activation on stratospheric aerosols and clouds in the Arctic polar vortex, Atmos. Chem. Phys., 12, 11095–11106, doi:10.5194/acp-12-11095-2012, 2012. 22113

Wohltmann, I., Wegner, T., Müller, R., Lehmann, R., Rex, M., Manney, G. L., Santee, M. L., Bernath, P., Sumińska-Ebersoldt, O., Stroh, F., von Hobe, M., Volk, C. M., Hösen, E., Ravegnani, F., Ulanovsky, A., and Yushkov, V.: Uncertainties in modelling heterogeneous chemistry and Arctic ozone depletion in the winter 2009/2010, Atmos. Chem. Phys., 13, 3909–3929, doi:10.5194/acp-13-3909-2013, 2013. 22111

NAT nucleation and denitrification in the Polar stratosphere

J.-U. Grooß et al.

Title Page

Abstract	Introduction
Conclusions	References
Tables	Figures

Back | Close

Full Screen / Esc

Printer-friendly Version

Interactive Discussion

Woiwode, W.: Qualification of the airborne FTIR spectrometer MIPAS-STR and study on denitrification and chlorine deactivation in Arctic winter 2009/10, Dissertation, Karlsruhe Insitute for Technology, Faculty of Chemistry and Biosciences, Karlsruhe, Germany, 2013. 22111, 22120

Table 1. Sensitivity simulations performed with CLaMS and corresponding labels. Different horizontal resolutions and assumptions for the NAT nucleation rate J are indicated.

label	resolution	description
HR	70 km	J (this work)
LR	100 km	J (this work)
X5	100 km	J (this work) ×5
T-1K	100 km	1 K lower temperatures, J (this work)
S64	100 km	higher density of particle parcels
Jconst	100 km	constant $J = 8 \times 10^{-6}\,\mathrm{cm}^{-3}\,\mathrm{h}^{-1}$
Jx10	100 km	constant $J = 8 \times 10^{-5}\,\mathrm{cm}^{-3}\,\mathrm{h}^{-1}$

Discussion Paper | Discussion Paper | Discussion Paper | Discussion Paper

Title Page

Abstract | Introduction

Conclusions | References

Tables | Figures

|◄ | ►|

◄ | ►

Back | Close

Full Screen / Esc

Printer-friendly Version

Interactive Discussion

Table A1. Reactions included into the CLaMS chemistry. Only the additional reactions are listed, which were not described by McKenna et al. (2002b), from which the bimolecular reactions (B1–B64), trimolecular or thermal decomposition reactions (T1–T12), photolysis reactions (J1–J27) and heterogeneous reactions (H1–H11) are used. Carbon and Fluorine containing products from halocarbon decomposition are neglected.

Nr	Reaction		
B65	$H + O_3$	$\rightarrow$	$OH + O_2$
B66	$H + HO_2$	$\rightarrow$	$OH + OH$
B67	$H + HO_2$	$\rightarrow$	$H_2O + O(^3P)$
B68	$H + HO_2$	$\rightarrow$	$H_2 + O_2$
B69	$H_2 + OH$	$\rightarrow$	$H_2O + H$
B70	$OH + O(^3P)$	$\rightarrow$	$H + O_2$
B71	$OH + OH$	$\rightarrow$	$H_2O + O(^3P)$
B72	$HO_2 + O(^3P)$	$\rightarrow$	$OH + O_2$
B73	$H_2O_2 + O(^3P)$	$\rightarrow$	$OH + HO_2$
B74	$O(^3P) + HOCl$	$\rightarrow$	$OH + ClO$
B75	$N_2O + O(^1D)$	$\rightarrow$	$N_2 + O_2$
B76	$N_2O + O(^1D)$	$\rightarrow$	$NO + NO$
B77	$CCl_3F + O(^1D)$	$\rightarrow$	$ClO + 2\,Cl + products$
B78	$CCl_2F_2 + O(^1D)$	$\rightarrow$	$ClO + Cl + products$
B79	$CHClF_2 + O(^1D)$	$\rightarrow$	$ClO + H + products$
B80	$CCl_3F_3 + O(^1D)$	$\rightarrow$	$ClO + 2\,Cl + products$
B81	$CCl_4 + O(^1D)$	$\rightarrow$	$3\,Cl + ClO + products$
B82	$CHClF_2 + OH$	$\rightarrow$	$Cl + H_2O + products$
B83	$CH_3Cl + OH\ (+O_2)$	$\rightarrow$	$ClO + CH_3OOH$
T13	$H + O_2 + M$	$\rightarrow$	HO_2
J28	$HCl + h\nu$	$\rightarrow$	$H + Cl$
J29	$H_2O + h\nu$	$\rightarrow$	$H + OH$
J30	$CCl_3F + h\nu$	$\rightarrow$	$3\,Cl + products$
J31	$CCl_2F_2 + h\nu$	$\rightarrow$	$2\,Cl + products$
J32	$CHClF_2 + h\nu$	$\rightarrow$	$Cl + H + products$
J33	$CCl_3F_3 + h\nu$	$\rightarrow$	$3\,Cl + products$
J34	$CH_3Cl + h\nu\ (+O_2)$	$\rightarrow$	$CH_3OO + Cl$
J35	$CCl_4 + h\nu$	$\rightarrow$	$4\,Cl + products$
J36	$N_2O + h\nu$	$\rightarrow$	$O(^1D) + N_2$

Title Page

Abstract | Introduction

Conclusions | References

Tables | Figures

|◄ | ►|

◄ | ►

Back | Close

Full Screen / Esc

Printer-friendly Version

Interactive Discussion

Table A2. Tracer correlations used in the initialisation procedure. The tracer correlations are derived from the observations using a polynomial fit of the form $[y] = \sum_{i=0}^{n} a_i \cdot [x]^i$ and degree $n \le 4$. The unit of CH_4 is ppmv, the units of N_2O, Cl_y, NO_y, and CO are ppbv and the unit of Br_y and halocarbons is pptv. For values of $[x]$ outside of the valid range, the closest valid value was used. The correlations are based on ACE-FTS version 3.0 data from October and November 2009 for equivalent latitudes above $50°$ N with the exception of Cl_y and Br_y that are taken from Grooß et al. (2005). The initialisation of $CFCl_3$ (CFC-11) is based on a wider range of equivalent latitudes (Φ_e) given in the third column (in degrees).

$[x]$	$[y]$	Range of Φ_e	Valid range of $[x]$	a_0	a_1	a_2	a_3	a_4
N_2O	CH_4		9.5…330	0.1917	0.01333	−8.239E-05	2.840E-07	−3.376E-10
ln N_2O	CH_4		ln 0.1…ln 9.5	0.1391	0.02516	0.01335	0.004192	0
CH_4	Cl_y		0.498…1.76	2.510	3.517	−3.741	0.4841	0.03042
CH_4	Br_y		0.65…1.64	48.73	−116.9	170.5	−102.1	19.58
N_2O	NO_y		49.6…330	11.57	0.1235	−1.013E-03	1.984E-06	−1.119E-09
ln N_2O	NO_y		ln 0.1…ln 49.6	7.988	1.338	0.1461	0	0
N_2O	CO		240…330	454.05	−8.8606	0.06614	−2.1697E-04	2.6421E-07
N_2O	CO		71…240	14.5	0	0	0	0
N_2O	CO		10…71	5.721	0.3647	−6.923E-03	6.855E-05	−2.656E-07
N_2O	CO		0…10	0	0.8740	0	0	0
N_2O	$CFCl_3$	60…90	204…312	−11.20	0.7959	−0.01413	8.508E-05	−1.278E-07
N_2O	$CFCl_3$	60…90	125…204	−12.15	0.6649	−8.777E-03	3.604E-05	0
N_2O	$CFCl_3$	60…90	100…125	−16.88	0.1688	0	0	0
N_2O	$CFCl_3$	40…60	147.5…326	−242.1	4.719	−0.04039	1.645E-04	−2.176E-07
N_2O	$CFCl_3$	20…40	169…320	−273.4	1.618	0	0	0
N_2O	$CFCl_3$	−10…10	216…314	−539.4	2.496	0	0	0
N_2O	CF_2Cl_2		30…312	−2.218	0.5757	7.425E-03	−1.285E-05	0
N_2O	CF_2Cl_2		0…30	0	0.7130	0	0	0
N_2O	CH_3Cl		200…330	−390	3.150	0	0	0
N_2O	CH_3Cl		100…200	−240	2.40	0	0	0
N_2O	$CHClF_2$		10…305.5	55.16	0.7999	−2.738E-03	5.400E-06	0
N_2O	$CHClF_2$		0…10	0	6.289	0	0	0
N_2O	CCl_4		190…330	−2.065	0.1238	−8.598E-04	4.805E-06	0
N_2O	CCl_4		120…190	−40.06	0.3339	0	0	0
N_2O	$C_2Cl_3F_3$		170…330	−83.69	0.4923	0	0	0
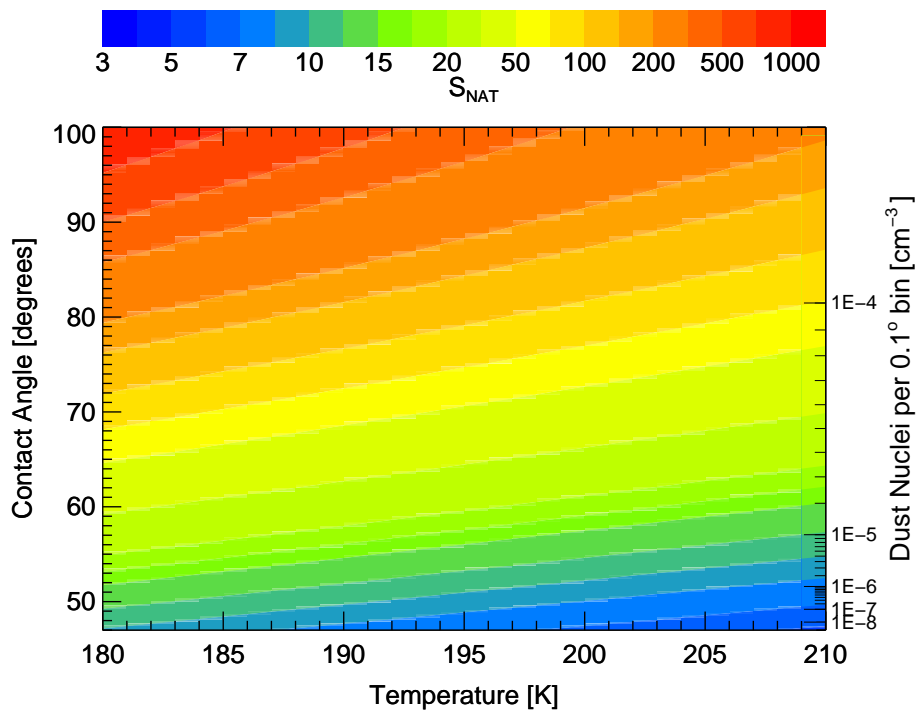
Fig. 1. Supersaturation needed for NAT nucleation for each 0.1° wide contact angle bin displayed as function of contact angle and temperature derived from Hoyle et al. (2013). The second vertical axis shows the corresponding number of dust particles per bin.
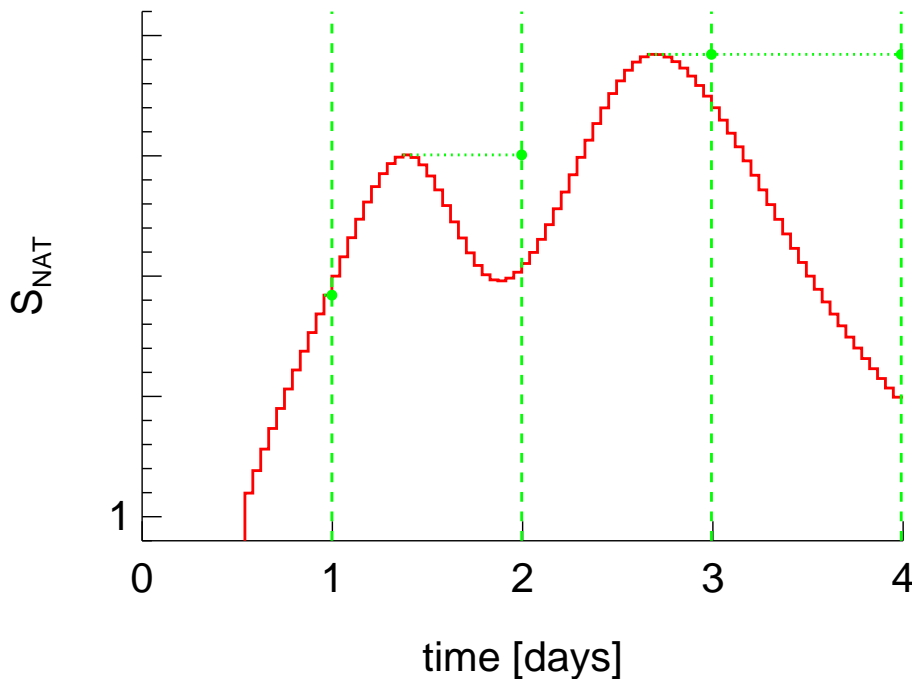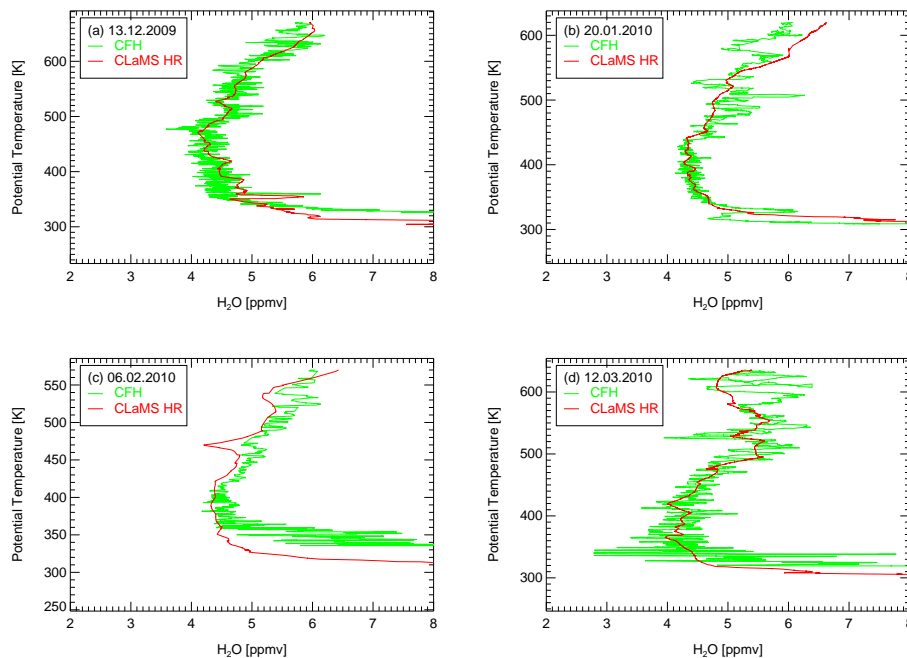
Fig. 2. Schematic of the determination of S_{NAT}^{max} along an exemplary air mass trajectory to demonstrate the principle of the parametrisation (no absolute values given). The red line corresponds to the hourly calculated values of S_{NAT} and the green dots indicate the derived value of S_{NAT}^{max} for each day of simulation.

Fig. 3. Comparison of CLaMS H_2O mixing ratios (red) with balloon borne CFH observations (green) made from Sodankylä for different times throughout the winter. Shown are ascent profiles from 13 December 2009, 20 January, 06 February, and 12 March 2010.

Discussion Paper | Discussion Paper | Discussion Paper | Discussion Paper

Full Screen / Esc

Printer-friendly Version

Interactive Discussion
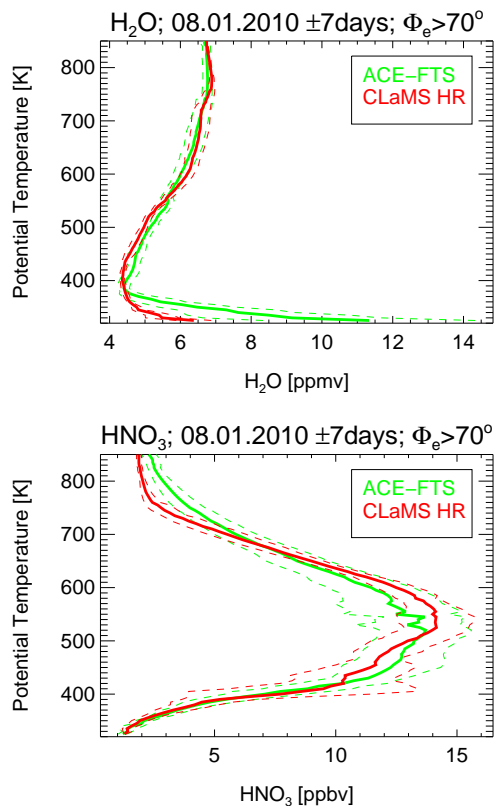
Fig. 4. Comparison of CLaMS H_2O and HNO_3 mixing ratios (red) with ACE-FTS observations (green). The ACE-FTS data is the average of all available data profiles within the time range of 8 January 2010 ± 7 days and with equivalent latitudes grater than 70° N. The dashed lines correspond to the standard deviation of the modelled and measured data (±1σ, red and green, respectively).

Title Page

Abstract | Introduction

Conclusions | References

Tables | Figures

|◄ | ►|

◄ | ►

Back | Close

Full Screen / Esc

Printer-friendly Version

Interactive Discussion
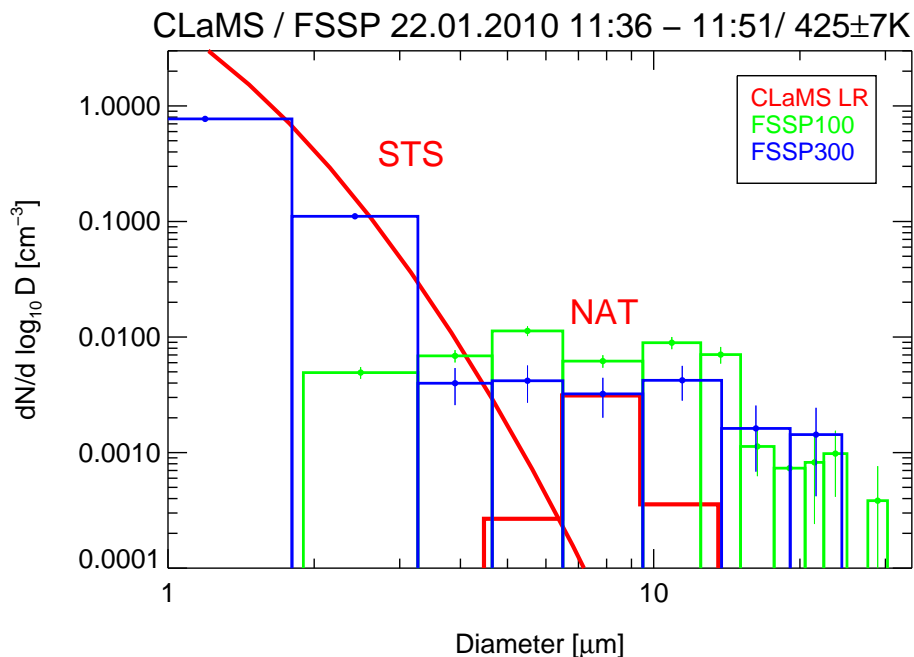
Fig. 5. Particle size distribution from FSSP observations on 22 January 2010. Shown are both FSSP-100 and FSSP-300 data for the flight segment between 11:36 and 11:51 UTC which had one of the largest particle concentrations during this campaign. The corresponding CLaMS particle size distribution (red) has two components, the liquid STS peak and the NAT particle combined from all CLaMS NAT particles within 100 km of the flight path segment.

Title Page

Abstract | Introduction

Conclusions | References

Tables | Figures

|◄ | ►|

◄ | ►

Back | Close

Full Screen / Esc

Printer-friendly Version

Interactive Discussion
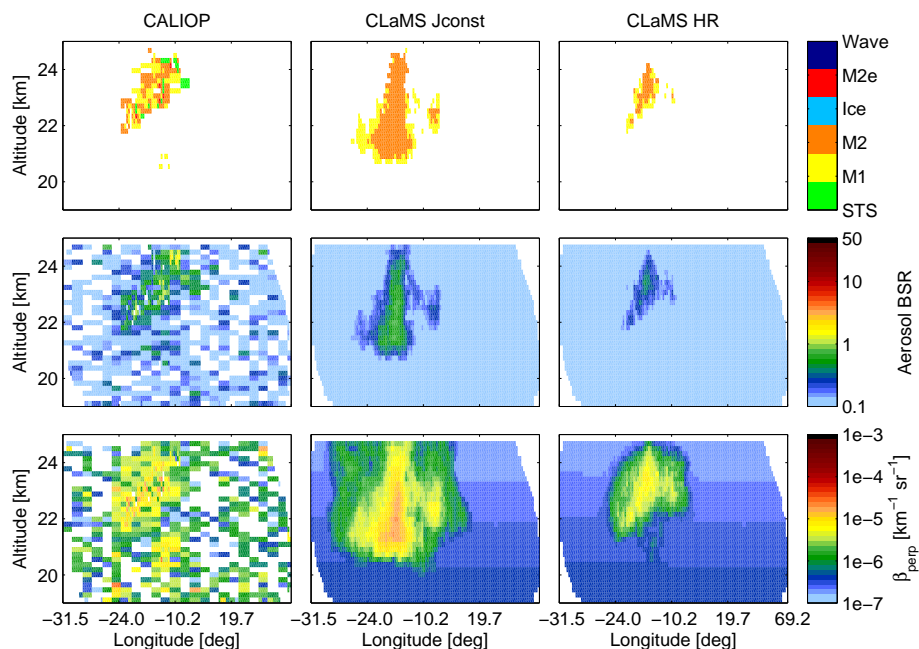
Fig. 6. CALIOP signals for one orbit segment on 21 December 2009, 04:54–04:55 UTC and corresponding T-matrix calculations from CLaMS results. The plots of left column show the CALIOP data whereas the corresponding CLaMS results for the runs Jconst and HR are shown in the middle and right columns, respectively. The panels in the top row show the particle classification after Pitts et al. (2009). The panels in the middle row correspond to the aerosol backscatter signal. The panels in the lower row correspond to the perpendicular backscatter signal.

Title Page

Abstract | Introduction

Conclusions | References

Tables | Figures

◄◄ | ►►

◄ | ►

Back | Close

Full Screen / Esc

Printer-friendly Version

Interactive Discussion
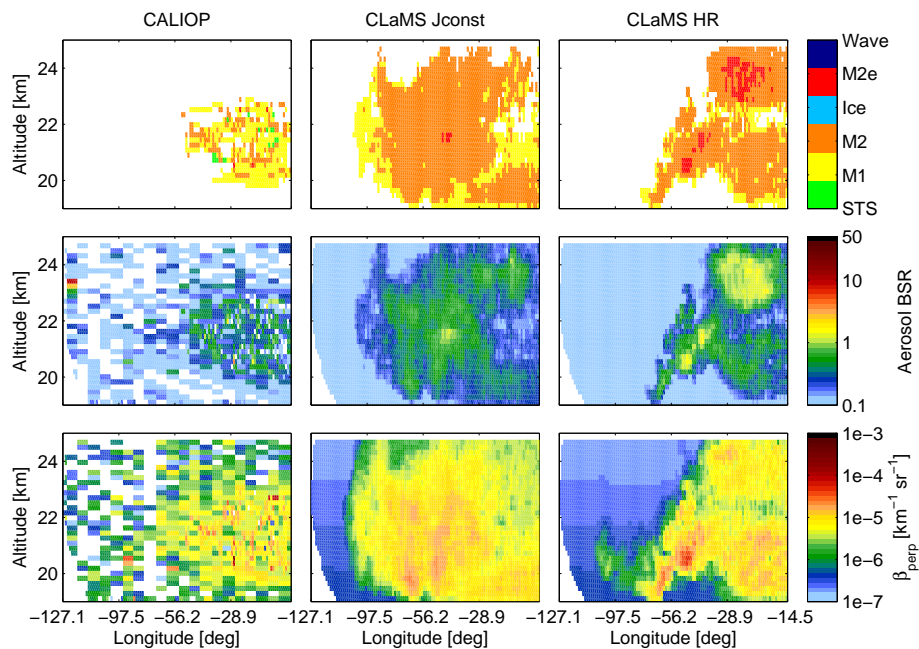
Fig. 7. As Fig. 6, but for 30 December 2009, 12:59 UTC.
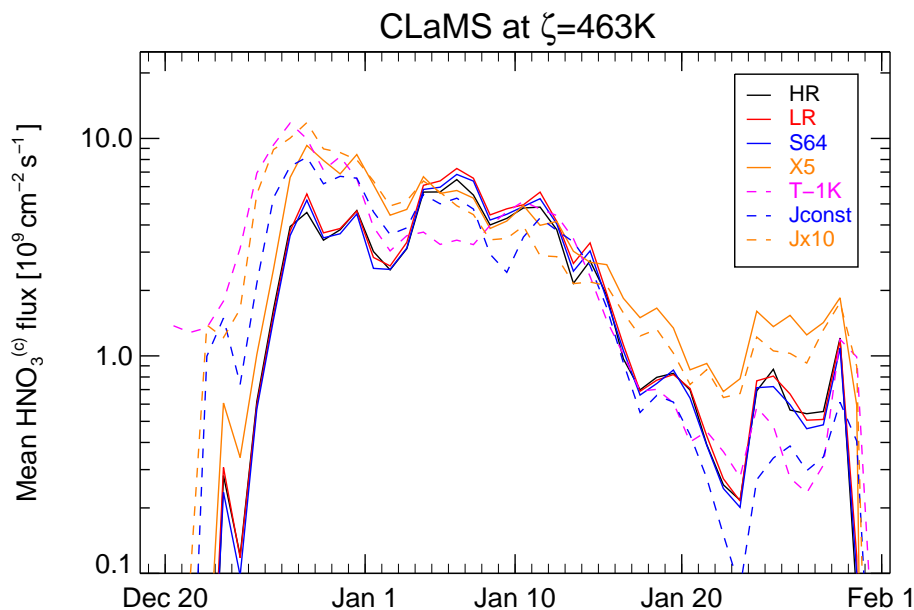
Fig. 8. Calculated mean HNO$_3$ flux within the model level at 463 K for the cold period between late December and end of January. Shown are the results for the different sensitivity simulations.
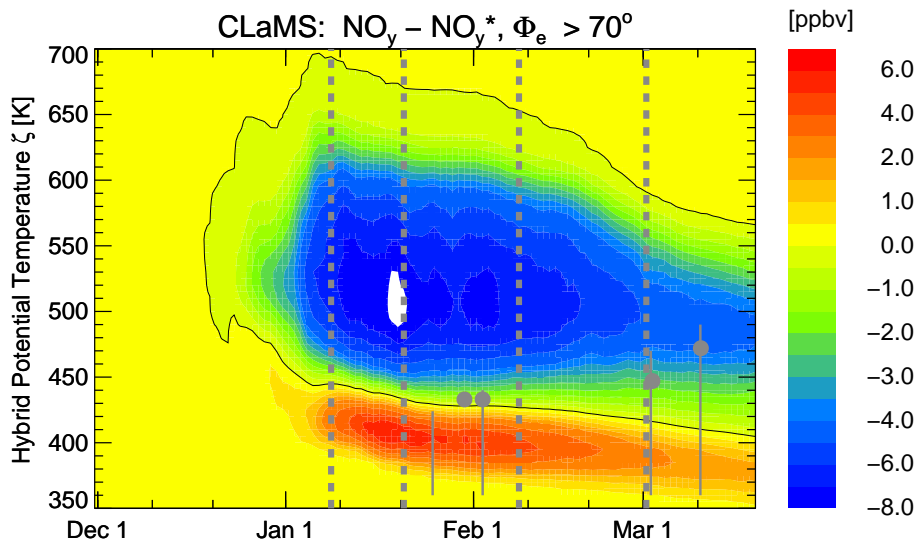
Fig. 9. Simulated NO_y redistribution from CLaMS HR run derived as the difference of simulated NO_y and the passive tracer NO_y^* averaged inside the polar vortex core (equivalent latitudes > 70° N). Dates where ACE-FTS comparisons are shown in Fig. 11 are marked as thick dashed grey lines. Comparisons with SIOUX on Geophysica shown in Figs. 12 and 13 are marked as grey dots and thin grey vertical lines, respectively.

Title Page

Abstract | Introduction

Conclusions | References

Tables | Figures

|◄ | ►|

◄ | ►

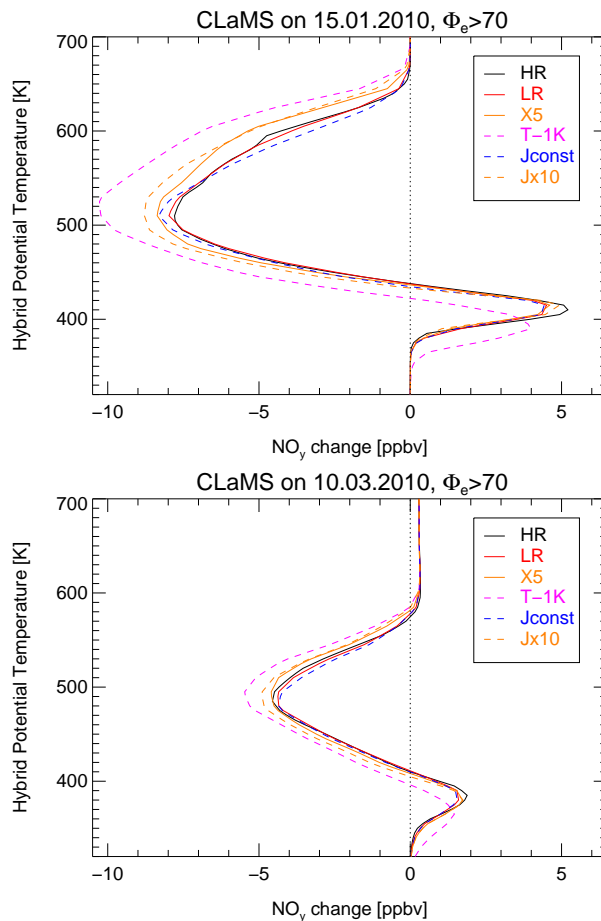Back | Close

Full Screen / Esc

Printer-friendly Version

Interactive Discussion

Fig. 10. Simulated NO_y redistribution profiles averaged inside the polar vortex core (equivalent latitudes > 70° N) for 15 January and 10 March. Shown are the results for the different sensitivity simulations as indicated in the legend. Simulation S64 that is almost identical with LR is omitted.
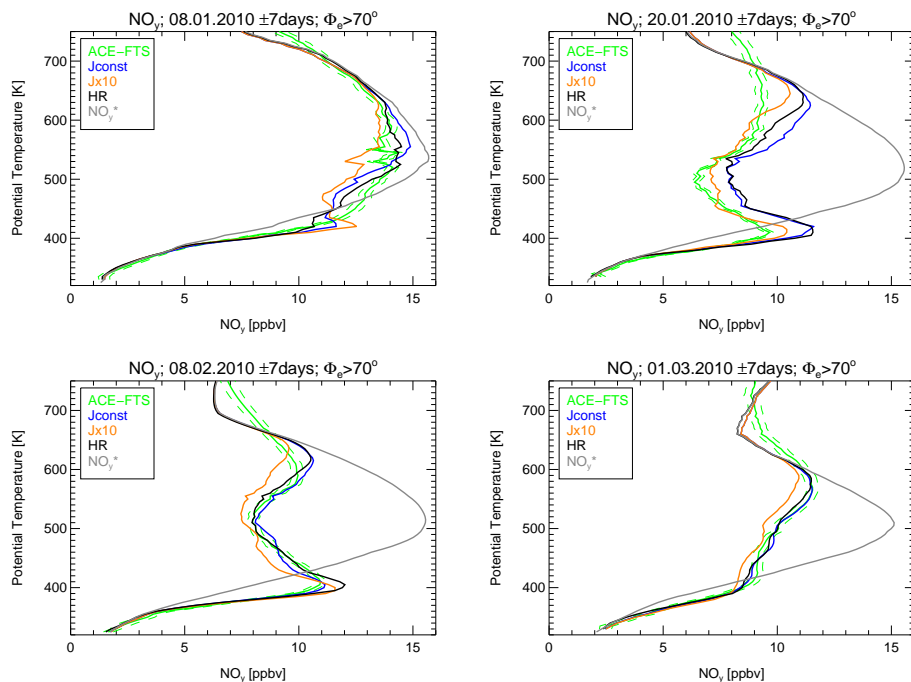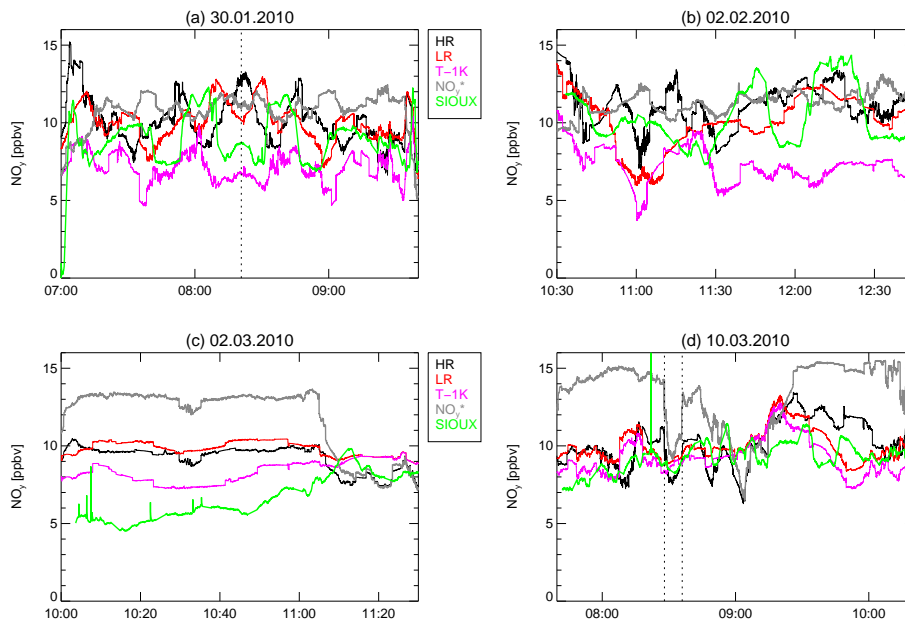
Fig. 11. Comparison of CLaMS NO_y mixing ratios with ACE-FTS data. For 4 different time ranges in which ACE-FTS observations are available in Northern polar latitudes, average NO_y profiles from ACE-FTS inside the polar vortex core (equivalent latitudes > 70° N) are shown (green lines). The accuracy of the NO_y data is indicated by the thin dashed green lines. The corresponding CLaMS results (HR) derived at the observation locations are shown in black. Also the simulation with constant nucleation rates (Jconst, Jx10) are shown as blue and orange lines, respectively. For comparison, the passive NO_y^* from CLaMS is shown as grey line.

Title Page

Abstract | Introduction

Conclusions | References

Tables | Figures

◄ | ►|

◄ | ►

Back | Close

Full Screen / Esc

Printer-friendly Version

Interactive Discussion
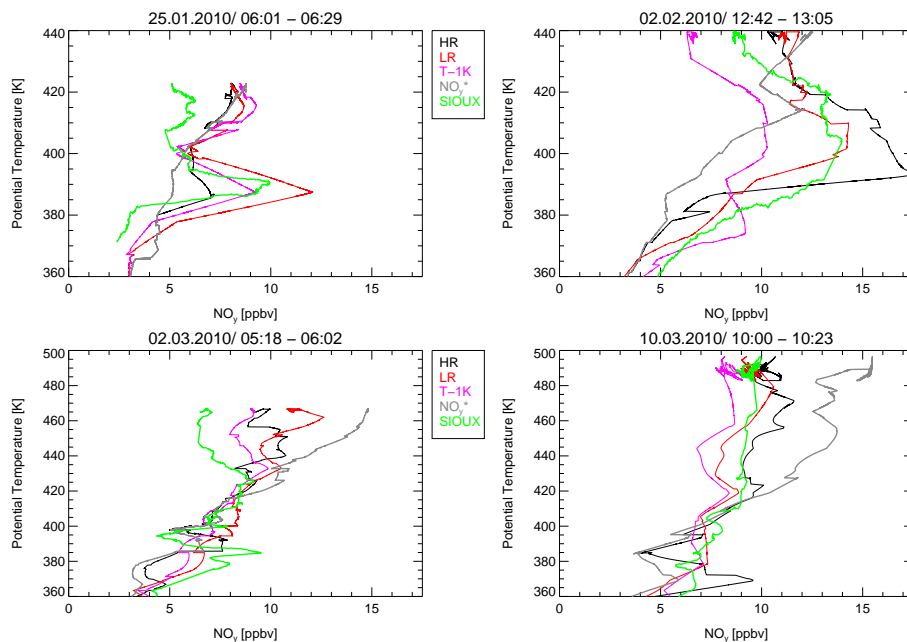
Fig. 12. Comparison of CLaMS NO_y mixing ratios with SIOUX data measured aboard the Geophysica aircraft. Shown are four time sections with NO_y observations inside the vortex for flights on 30 January, 2 February, 2 March and 10 March 2010. SIOUX data are displayed as green lines. CLaMS results are displayed for 3 different simulations, the high resolution (HR, black), the low resolution (LR, red), and the simulation with 1 K temperatures decrease (T-1K, pink). The passive NO_y^* from CLaMS is shown as grey line. The average potential temperature of the flight segments is 432 K, 433 K, 447 K, and 472 K, respectively. In panel a the turnaround time and in panel d the observation of a filament of extra-vortex air in the vortex are marked with dotted lines.

Title Page

Abstract | Introduction

Conclusions | References

Tables | Figures

Back | Close

Full Screen / Esc

Printer-friendly Version

Interactive Discussion

Fig. 13. Comparison of CLaMS NO_y mixing ratio profiles with SIOUX data measured aboard the Geophysica aircraft. Four profiles are shown with NO_y observations inside the vortex for different flights (for date and times see panel titles). SIOUX data are displayed as green lines. CLaMS results are displayed for 3 different simulations, the high resolution (HR, black), the low resolution (LR, red), and the simulation with 1 K temperatures decrease (T-1K, pink). The passive tracer NO_y^* from CLaMS is shown as a grey line.

Title Page

Abstract | Introduction

Conclusions | References

Tables | Figures

◀ | ▶|

◀ | ▶

Back | Close

Full Screen / Esc

Printer-friendly Version

Interactive Discussion